Predicting surface dynamic topographies of stagnant lid planetary bodies

Caroline Dumoulin, O Čadek, Gael Choblet

Geophysical Journal International

Geophys. J. Int. (2013) doi: 10.1093/gji/ggt363

Geophysical Journal International Advance Access published October 3, 2013

Predicting surface dynamic topographies of stagnant lid planetary bodies

C. Dumoulin,[1] O. Čadek[2] and G. Choblet[1]

[1] *Université de Nantes, Laboratoire de Planétologie et Géodynamique, CNRS-UMR*6112*, France. E-mail: caroline.dumoulin@univ-nantes.fr*
[2] *Department of Geophysics, Faculty of Mathematics and Physics, Charles University, Prague, Czech Republic*

Accepted 2013 September 5. Received 2013 September 3; in original form 2013 April 29

SUMMARY

Although planetary mantles are viscoelastic media, numerical models of thermal convection in a viscoelastic spherical shell are still very challenging. Here, we examine the validity of simplified mechanical and rheological frameworks classically used to approximate viscoelastic dynamic topography. We compare three simplified approaches to a linear Maxwell viscoelastic shell with a pseudo upper free-surface, considered as the reference model. A viscous model with a free-slip boundary condition at the surface correctly reproduces the final relaxed shape of the viscoelastic body but it cannot reproduce the time evolution of the viscoelastic topography. Nevertheless, characterizing the topography development is important since it can represent a significant fraction of the history for planets having a thick and rigid lithosphere (e.g. Mars). A viscous model with a pseudo free-surface, despite its time-dependency, also systematically fails to describe correctly these transient stages. An elastic filtering of the instantaneous viscous topography is required to capture the essence of the time evolution of the topography. We show that a single effective elastic thickness is needed to correctly reproduce the constant transient viscoelastic topography obtained when the lithosphere corresponds to a step-like viscosity variation, while a time-dependence of the effective elastic thickness must be considered to take account of realistic temperature-dependent viscosity variations in the lithosphere. In this case, the appropriate thickness of the elastic shell can be evaluated, at a given instant, with a simple procedure based on the local Maxwell time. Furthermore, if the elastic filtering is performed using the thin elastic shell formulation, an unrealistic degree-dependence of the thickness of the elastic shell is needed to correctly approximate the viscoelastic topography. We show that a model that fully couples a viscous body to an elastic shell of finite thickness estimated using the local Maxwell time gives the best approximation of the viscoelastic deformation, whatever the degree of the load and the time of loading.

Key words: Lunar and planetary geodesy and gravity; Dynamics of lithosphere and mantle; Lithospheric flexure; Planetary interiors.

1 INTRODUCTION

Thermal convection in planetary mantles leads to surface dynamic topography by means of viscoelastic deformation of the lithosphere. In the case of several terrestrial planets, topography is now known with a high resolution thanks to orbiting altimeters (Wieczorek 2007). Identifying the dynamic contribution to this observation remains nevertheless complex. A way to constrain this dynamic part is to compute the free-surface deformation resulting from mantle flows together with the associated geoid anomalies. In order to evaluate the surface dynamic topography, it is often necessary to introduce a specific treatment for the deformation of the lithosphere. Understanding the consequences of the rheological and mechanical approximations related to this treatment is therefore a key issue.

Models of viscoelastic convection in the whole mantle are mainly developed in 2-D geometries (e.g. Harder 1991; Zhong *et al.* 1996; Muhlhaus & Regenauer-Lieb 2005; Gerya & Yuen 2007; Beuchert & Podladchikov 2010). Since fully 3-D-spherical thermal convection in a viscoelastic medium is still very challenging, most of the studies concerning dynamic topography of planetary surfaces use a simplified rheological set-up. Following the pioneer work of Ricard *et al.* (1984) and Richards & Hager (1984) for the Earth, numerous studies have been dedicated to the computation of dynamic topography and geoid using instantaneous viscous flow models [e.g. Mars: Harder & Christensen (1996), Harder (2000) and Redmond & King (2004); Venus: Benešová & Čížková (2012) and Huang *et al.* (2013); Mercury: Redmond & King (2007)]. Richards & Hager (1984) showed that, in the case of a thin lithosphere a 100 times more viscous than the underlying mantle, viscous

relaxation times are small enough to be neglected when compared to the timescales inherent to convective processes. The surface dynamic topography is then supposed to be generated instantaneously by mantle flow. When the lithosphere is stiff and thick, it acts as an elastic filter reducing the amplitude of the surface dynamic topography. In the case of Mars, Zhong (2002) showed that, owing to the lithospheric rigidity, the viscoelastic response exhibits a transient stage before reaching the relaxation of viscous stresses. This plateau-like transient stage could prevail over a significant fraction of the planet's history. Hybrid models involving a coupling between viscous and elastic deformations have been implemented in order to take into account this effect, particularly to evaluate the contribution of an hypothetical plume below the Tharsis rise to the present-day topography and geoid (Zhong 2002; Lowry & Zhong 2003; Zhong & Roberts 2003; Roberts & Zhong 2004; Golle *et al.* 2012).

Earlier studies on surface topography generated by internal loads typically used a step-like structure to describe the radial variations of viscosity associated with thermal and mineralogical changes in the lithosphere (e.g. Ricard *et al.* 1984; Richards & Hager 1984; Wu & Peltier 1982; Zhong *et al.* 1996; Zhong 2002). This choice was motivated mainly by reasons of simplicity. In this paper, we investigate the effect of a more realistic viscosity profile. In the context of a generic one-plate planetary body, the two most important parameters influencing radial variations of mantle viscosity (especially in the uppermost part including the lithosphere) are (i) temperature and, although less well constrained and (ii) composition (such as water content).

Even though little is known about activation energies for the Earth's lower mantle rocks, and although precise values are still debated even for olivine (*cf.* e.g. Korenaga & Karato 2008), it is generally accepted that deformation of mantle polycrystals is a thermally activated process. As a consequence, planetary lithospheres, as cold boundary layers of convecting mantles in the stagnant lid regime, that are the loci for temperature differences of several hundreds of Kelvins, host continuous viscosity variations of several orders of magnitude. In the case of the Earth, the effect of (de-)hydration on the rheology of olivine crystals is considered to contribute to a strong viscosity stratification of the water saturated oceanic mantle experiencing partial melting (and thus dehydration) beneath spreading centres (Hirth & Kohlstedt 1996). Similarly, it has been proposed that continental roots survive for several billions of years due to the removal of water by partial melting (e.g. Jordan 1978; Sleep 2003). The exact magnitude of this effect in terms of viscosity contrast naturally depends on the water content (and thus on the geodynamic context) and experimental data might still be equivocal with this regard: from two orders of magnitude in the context of mid ocean ridges (Hirth & Kohlstedt 1996) up to four orders of magnitude in the case of continental roots (Karato 2010).

In this work, these two effects are described through their impact on the radial viscosity profile. Although the magnitude of the dehydration effect is smaller and its occurrence is not systematic, the fact that the transition from dry and viscous lithosphere to wet and less viscous mantle is sharp, contrasts with the gradual variation of viscosity throughout the lithosphere (if the conductive temperature profile increases linearly with depth in the lithosphere, the logarithm of viscosity also decreases linearly). We therefore consider two groups of viscosity profiles corresponding to the two end-members.

On Earth, lithospheric viscosity is even more problematic to constrain, because of the occurrence of plate tectonics. Deformation occurs mainly at plate boundaries, inducing a low effective viscosity, while viscosity is supposed to be large in cold and tectonically non-active regions (shields and cratons, see e.g. Čadek & Fleitout 2003). We therefore focus our study on the dynamic topography of stagnant lid planetary bodies. In the following, models are sufficiently general to be appropriate for any stagnant lid planetary body but the dimensions of Mars and material properties typical of rocks are used (Table 1). Mantle and core densities are chosen so that the gravitational acceleration at the surface equals Mars' value.

In the following two sections, we present the various categories of viscosity profiles considered in this study and describe the available approaches to model the viscous and the viscoelastic deformation in 3-D spherical geometry. We then compare these models in terms of

Table 1. Physical and geometrical model parameters.

Symbol	Parameter	Value
	Mars-like planet	
R_s	Outer radius	3400 km
R_c	Radius at the CMB	1700 km
g_s	Gravitational acceleration at the surface	3.77 m s^{-2}
μ	Shear modulus	7×10^{10} Pa
ρ_m	Mantle density	3400 kg m^{-3}
ρ_c	Core density	8000 kg m^{-3}
	Viscosity profile	
z_{lid}	Lid thickness	100–500 km
E_a	Activation energy	240 kJ mol^{-1}
H	Internal heating rate	3×10^{-12} to 14×10^{-12} W kg^{-1}
T_s	Surface temperature	220 K
T_i	Internal temperature	1650 K
k	Thermal conductivity	4 W $m^{-1}K^{-1}$
η_i	Internal dynamic viscosity	10^{20} Pa s
η_{max}	Maximum dynamic viscosity	10^{30} Pa s

predicted dynamic topography. A single degree 2 load located at mid-depth is first considered. We then vary the harmonic degree (up to degree 30) and the depth of the load. In a more realistic set-up, we finally compute the dynamic topography over a synthetic stable plume.

2 VISCOSITY STRUCTURE

We consider here two families of viscosity profiles including the effects of radial variations in temperature and composition. For the sake of simplicity, the dependence of viscosity on grain size, pressure and strain rate is neglected.

2.1 Thermal effect

The first group of viscosity profiles describe the thermal effect: a radially dependent effective viscosity is computed from a synthetic temperature profile $T(r)$ using the Arrhenius law

$$\eta(r) = \eta_{\rm ref} \exp\left[\frac{E_{\rm a}}{RT(r)}\right], \quad (1)$$

where $E_{\rm a}$ is the activation energy, R is the universal gas constant, and $\eta_{\rm ref}$ the reference viscosity chosen such that the deep mantle viscosity equals 10^{20} Pa s (see Table 1 and Fig. 1). The average temperature profile $T(r)$ is associated with internally heated stagnant lid convection in a spherical shell, as described by Reese *et al.* (2005). Since we focus our analysis on a thermal steady-state and do not intend to describe the thermal evolution of planetary bodies, the temperature profile is assumed to be independent of time.

Given a stagnant lid thickness ($z_{\rm lid}$), an activation energy, a surface temperature $T_{\rm s}$, an internal heating rate H, and a thermal conductivity value k, the scaling relationships proposed by Reese *et al.* (2005) describe the temperature profile in a stagnant lid [i.e. $T(r)$ for $r > R_s - z_{\rm lid}$, with R_s the outer radius], the internal temperature $T_{\rm i}$ as well as the thickness δ of the rheological sublayer (i.e. the layer below the stagnant lid that gives birth to cold instabilities). The internal heating rate is chosen so that $T_{\rm i} = 1650$ K, whatever the thickness of the rigid lid. For a radius smaller than $R_{\rm s} - z_{\rm lid} - 2\delta$, temperature is equal to $T_{\rm i}$, and for $R_{\rm s} - z_{\rm lid} > r > R_{\rm s} - z_{\rm lid} - 2\delta$, T follows a parabola from $T_{\rm L}$ to $T_{\rm i}$. Fig. 1 shows the temperature profiles obtained for various thicknesses of the lid (left-hand panel), together with the corresponding viscosity profiles (right-hand panel).

For numerical reasons, a cut-off value of 10^{30} Pa s is introduced when computing the first group of viscosity profiles. This cut-off viscosity shall also be envisioned as a cut-off strength of the lithosphere: even if the generic lithosphere we consider does not encounter plate tectonics (so that its strength might be larger than the one of the Earth's lithosphere), mechanisms such as brittle failure or other weakening processes will act to limit the strength for regions corresponding to low temperatures, where the concept of viscous lithosphere is probably not relevant. Depending on the thickness of the lid, the thickness of the layer below the surface where this cut-off viscosity is prescribed varies from 41 to 201 km in our models (see Fig. 1).

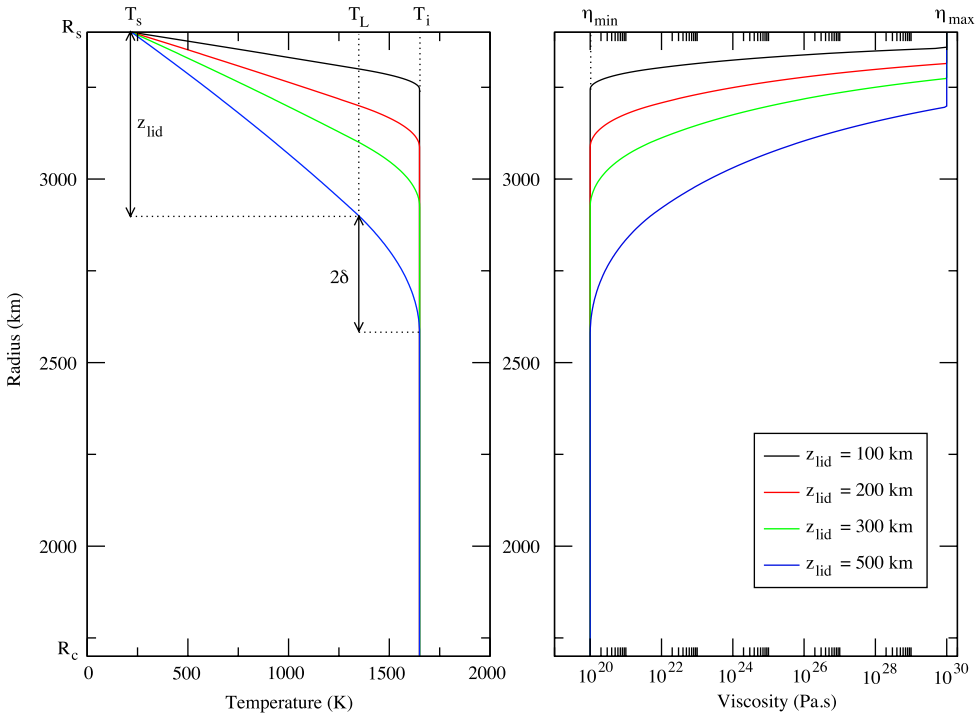

Figure 1. Temperature profiles (left-hand panel) computed using scaling laws proposed by Reese *et al.* (2005) for stagnant lid convection. Viscosity profiles (right-hand panel) derived from the temperature profiles (see text for more details) and used in our viscoelastic and viscous models.

2.2 Lithospheric dehydration effect

Since the compositional boundary caused by the removal of water is potentially very sharp, we mimic this effect by a step-like viscosity structure, comparable to the ones used by earlier studies (e.g. Wu & Peltier 1982; Zhong *et al.* 1996; Zhong 2002). Little is known about the water content of planetary mantles. Here, we consider viscosity contrasts up to 10 orders of magnitude, hence much larger than those induced by dehydration in olivine. The cases with a step-like viscosity structure presented below shall be viewed both as a mean to compare our work to earlier studies, and as an upper limit of a possible rheological stratification caused by dehydration of the lithosphere. In addition, note that the two end-member viscosity structures considered in this study are not equally likely: while the exponential profile caused solely by a thermal effect is a plausible end-member, the step-like profile end-member is less likely since the thermal effect in the lithosphere cannot be suppressed.

3 MODELS DESCRIPTION

In this section, we describe the three different approaches used to compute the dynamic topography induced by an internal load. All models presented here use semi-spectral methods with an identical radial discretization. Loading is performed in a similar manner for each model: a mass anomaly of a given degree (from $\ell = 2$ to 30) is imposed at a given depth. We use a Heaviside function for the loading history, that is, the load is applied at time $t = 0$ and remains the same for $t > 0$, as in Zhong (2002).

3.1 Viscoelastic model

In order to understand how to approximate dynamic topographies that develop at the surface of viscoelastic bodies, we first compute response functions using a viscoelastic model. The response of an incompressible planet to internal loads is governed by the equations of mass and momentum conservation:

$$\nabla \cdot \boldsymbol{v} = 0, \tag{2}$$

$$-\nabla p + \nabla \cdot \boldsymbol{\tau} + \boldsymbol{f} = \boldsymbol{0}, \tag{3}$$

with $\boldsymbol{v}$ the velocity, p the dynamic pressure, $\boldsymbol{\tau}$ the deviatoric part of the stress tensor and $\boldsymbol{f}$ the body force. Because its effect on dynamic topography (but not on the convective flow) is likely to be important at low degrees (Ricard *et al.* 1984), self-gravitation is considered. The body force is then expressed as follows:

$$\boldsymbol{f}(r, \theta, \phi) = \delta\rho(r, \theta, \phi)\boldsymbol{g}(r) + \rho_{\mathrm{m}}\nabla V(r, \theta, \phi), \tag{4}$$

where ρ_{m} is the mean mantle density, $\boldsymbol{g}$ is the mean gravitational acceleration at a given radius, $\delta\rho$ denotes perturbations of density and V stands for the variations of the gravitational potential. Note that the gravitational acceleration $\boldsymbol{g}$ is computed in a way consistent with the chosen internal structure of the planetary body (see Table 1).

We consider a linear incompressible Maxwell body,

$$\dot{\boldsymbol{\epsilon}} = \frac{1}{2\eta}\boldsymbol{\tau} + \frac{1}{2\mu}\frac{\partial \boldsymbol{\tau}}{\partial t}, \tag{5}$$

where $\dot{\boldsymbol{\epsilon}}$ is the strain rate tensor, η is the effective viscosity and μ is the shear modulus. We are aware that the linearized Maxwell viscoelasticity may not be an appropriate material approximation in a plate tectonic context where the partial time derivative of the stress tensor is usually replaced by a convective (or invariant) derivative including also non-linear advection and corotation terms (as in Harder 1991; Muhlhaus & Regenauer-Lieb 2005; Kaus & Becker 2007; Beuchert & Podladchikov 2010). In specific geodynamic settings, such as for example, subduction zones, these terms play a non-neglibible role and cannot be omitted (Muhlhaus & Regenauer-Lieb 2005; Kaus & Becker 2007; Beuchert & Podladchikov 2010). In the stagnant lid context of our experiments, we have nevertheless estimated possible effects of stress advection on the viscoelastic flow driven in mantle by long-wavelength loads by performing several tests using our spectral solver. We considered various radially stratified viscosity models and computed the solution of eqs (2)–(5) without and with the advection term [in the latter case, an additional non-linear term $(2\mu)^{-1}\boldsymbol{v}.\nabla\boldsymbol{\tau}$ was included in the right-hand side of eq. 5]. We performed a series of calculations for different low ($\ell < 20$) degree density structures with amplitudes similar to those expected in the Earth's mantle. For all these calculations we found that the solutions with and without the advection term were almost identical during the whole time evolution, which indicates that the stress advection can be neglected in these applications. Concerning the rotational terms, Muhlhaus & Regenauer-Lieb (2005) showed that they are only important for very large values of stress. For density and viscoelastic structures of a planetary mantle that do not vary with time, the response asymptotically approaches a steady-state value. As a consequence of the chosen formulation of the constitutive equation, the viscoelastic steady-state response is identical to the viscous limit.

Pseudo free-surfaces are considered on the boundaries (at $r = R_{\mathrm{s}}$, the outer radius, and $r = R_{\mathrm{c}}$, the core–mantle boundary): topography is updated using the radial velocity on the pseudo free-surface and then applied as boundary-normal stress on the top or bottom of our domain when updating the velocity (e.g. Zhong *et al.* 1996). Tangential components of the traction at the surface are set to zero. This approach assumes that the surface remains close to the spherical shape (Ricard 2007), which is relevant for planetary bodies.

Eqs (2)–(5) can be discretized in time using a simple implicit time scheme (e.g. Schmalholz *et al.* 2001; Zhong *et al.* 2003; Gerya & Yuen 2007):

$$\nabla \cdot \boldsymbol{v}^{(n)} = 0, \tag{6}$$

$$-\nabla p^{(n)} + \nabla \cdot \boldsymbol{\tau}^{(n)} = -\delta\rho \boldsymbol{g} - \rho_m \nabla V^{(n-1)}, \tag{7}$$

$$\boldsymbol{\tau}^{(n)} \left(\frac{1}{2\eta} + \frac{1}{2\mu\Delta t} \right) - \dot{\boldsymbol{\epsilon}} = \frac{1}{2\mu\Delta t} \boldsymbol{\tau}^{(n-1)}, \tag{8}$$

where superscripts n and $n-1$ denote the quantities in the nth and $n-1$st time step, respectively, and $\Delta t = t^{(n)} - t^{(n-1)}$. The left-hand sides of eqs (6)–(8) are formally identical to the equations governing static deformation of an incompressible elastic body in which the displacement vector and the shear modulus are replaced by velocity $\boldsymbol{v}$ and the term $[1/\eta - 1/(\mu\Delta t)]^{-1}$, respectively. Eqs (6)–(8) can thus be easily solved by a spectral solver developed for elastic deformation provided that μ and η are only functions of radius. Here we use the method described in Golle *et al.* (2012) in which we modified the boundary conditions and the right-hand side vector. Our method has been benchmarked against the Laplace domain solution for a step-like viscosity profile (Zhong 2002) and, for surface loading and a continuous viscosity profile, against the spectral-finite element code of Martinec (2000).

3.2 Viscous models

We consider two viscous models whose predictions will be compared to the results of the viscoelastic model described above: in this case, eqs (2) and (3) are solved together with the constitutive equation for a viscous medium:

$$\dot{\boldsymbol{\epsilon}} = \frac{1}{2\eta} \boldsymbol{\tau}. \tag{9}$$

The surface mechanical boundary condition is either a pseudo free-surface, computed in the same way as in the viscoelastic model, or a free slip, that is, zero radial velocity and zero tangential component of traction. As opposed to the viscous model with a free upper surface (VF-FS), this last model does not involve any time evolution (since we use a step-function loading history) and is therefore usually referred to as the instantaneous viscous flow model (IVF). In the IVF model, the normal stress generated by internal buoyancy is instantaneously compensated by surface dynamic topography, here defined as a deviation from the sphere of radius R_s:

$$h_{\ell m}^{\mathrm{IVF}} = -\frac{[\sigma_{rr}(R_{\mathrm{s}})]_{\ell m}}{\rho_{\mathrm{m}} g_{\mathrm{s}}}, \tag{10}$$

where the subscript ℓm denotes spectral decomposition (see Golle *et al.* 2012, for more details). Surface dynamic topography generated with the IVF model then corresponds to the steady-state response of both viscoelastic and viscous free-surface models.

3.3 Elastic filtering of the viscous response

As stated in Zhong (2002), an elastic filtering may be applied on the IVF response in order to approximate a viscoelastic transient response. Indeed, Zhong (2002) showed that for a specific viscous structure (a 100-km-thick layer with a viscosity 10^6 times larger than the underlying mantle) and for a degree 2 load, the steady-state response is reached for times greater than 10^9 yr. However, at shorter times, the viscoelastic topography displays a constant transient response that can be modelled applying an elastic filter to the IVF response. This elastic filtering can be performed in two different ways: (i) the surface dynamic topography obtained with the IVF model is applied as a load at the surface of a thin elastic shell (Zhong 2002; Roberts & Zhong 2004) using the thin elastic shell approximation (Turcotte *et al.* 1981), called IVF-TES model in the following, or (ii) a viscous shell is coupled to an elastic shell by means of the traction that arises from the viscous flow [called ESW, as elastic shell within, in the following, see Golle *et al.* (2012) for details]. The elastic thin shell theory applies if the following conditions are satisfied: the shell is thin compared to its radius, deflections are small compared to the shell radius, and the shell thickness is much smaller than the horizontal dimension of the load (for more details, see Kraus 1967; Beuthe 2008; Kalousová *et al.* 2012). The structure of the ESW model (i.e. the load of an elastic shell from below by means of the viscous traction evaluated at depth) can be expected to be more robust than the structure of the IVF-TES model. It also allows for more complex developments (such as radial variations of rheological parameters in the elastic shell for example). On the other hand, the IVF-TES model is easy to compute and the elastic thin shell approximation can be extended to take into account lateral variations of elastic thickness (Beuthe 2008; Kalousová *et al.* 2012).

Using the IVF-TES model, the filtered surface topography can be computed as

$$h_{\ell m}^{\mathrm{IVF-TES}} = C_\ell h_{\ell m}^{\mathrm{IVF}}, \tag{11}$$

where C_ℓ is the degree of compensation at harmonic degree ℓ [derived by Turcotte *et al.* (1981) and modified by Willemann & Turcotte (1982)]:

$$C_\ell = \left[1 - \frac{3\rho_m}{(2\ell+1)\bar{\rho}} \right] \left\{ \frac{\sigma[\ell^3(\ell+1)^3 - 4\ell^2(\ell+1)^2 + 4\ell(\ell+1)] + \tau[\ell(\ell+1) - 2] + \ell(\ell+1) - (1-\nu)}{\ell(\ell+1) - (1-\nu)} - \frac{3\rho_m}{(2\ell+1)\bar{\rho}} \right\}^{-1}, \tag{12}$$

Here, $\bar{\rho}$ is the mean density of the planet, ν is the Poisson ratio ($\nu = 0.5$ since we assume an incompressible fluid), τ is a measure of the rigidity of the spherical shell if bending resistance is neglected,

$$\tau = \frac{2\mu(1+\nu)T_e}{R_s^2 g_s \rho_m}, \tag{13}$$

with T_e being the elastic shell thickness, and σ a measure of the resistance of the shell to bending,

$$\sigma = \frac{\tau}{12(1-\nu^2)}\left(\frac{T_e}{R_s}\right)^2. \tag{14}$$

In the second model (ESW), an elastic shell of finite thickness is introduced. The viscous flow develops in the whole spherical domain (mantle and lithosphere) and the traction prescribed at the bottom of the elastic shell is computed from the stress field at the depth corresponding to the elastic thickness. The elastic deformation is, as the viscous one, computed using a semi-spectral model (for more details, see Golle *et al.* 2012). Note that, in Golle *et al.* (2012), a no-slip condition is applied at the surface boundary of the viscous model. In this study, a free-slip condition has been introduced because the thickness of the stress boundary layer generated by such a condition is not negligible compared to the effective elastic thicknesses investigated here ($\simeq$50–300 km). We also improved Golle *et al.* (2012)'s model by adding the self-gravitation. The viscous shell is discretized by 499 cells in the radial direction. Consequently, the elastic thickness in this model can only be increased by an increment of 3.4 km.

4 COMPARISON OF VISCOELASTIC RESPONSES WITH SIMPLIFIED APPROACHES

We have presented above four different models that can be used to approximate the accurate dynamic topography inferred by the viscoelastic rheology. In order to determine their efficiency, we systematically compare the dynamic topography they predict to the viscoelastic deformation. Three approaches are used: a viscous flow with a free surface (VF-FS model) or with a free-slip upper boundary (IVF model), and an instantaneous viscous flow filtered by an elastic lithosphere. For this last approach, two models are envisioned: the IVF topography is filtered using the thin elastic shell approximation (IVF-TES model) or through the coupling of a viscous shell to an elastic shell (ESW model).

First, we solve for the flow induced by a degree 2 mass anomaly located at mid-mantle depth. We then generalize the analysis to other harmonic degrees and consider two locations (one at mid-mantle depth, one beneath the lithosphere). Finally, a more realistic set-up corresponding to a stable synthetic plume is considered.

4.1 Degree 2 load located at mid-mantle depth

We first consider results obtained for a step-like viscosity profile, as in most of the previous studies about viscoelastic topographies (e.g. Wu & Peltier 1982; Zhong *et al.* 1996; Zhong 2002). As previously noted by Zhong (2002), characteristic times of viscoelastic models only depend on the mechanical structure and harmonic degree for a given mantle viscosity: the time needed to reach the steady-state increases with increasing viscosity contrast between the mantle and the lithosphere. Fig. 2 displays time-dependent response in surface topography normalized by the IVF (asymptotic steady-state) response. A degree-2 load is prescribed at mid-mantle depth at $t = 0$. The steady-state is obtained after 4×10^8 yr for a two-layers case with a viscosity contrast of 10^6 over 201 km, after 2×10^{12} yr for a viscosity contrast of 10^{10} over 82 km (red and green curves, respectively).

As indicated above, the cold thermal boundary layer that develops at the surface of planetary mantles is associated with very large viscosities so that the steady state viscoelastic topography will only be reached at times much larger than convective ones (also possibly larger than the age of the Solar System or the Universe). For this reason, Zhong (2002) concluded that the observed dynamic topography of Mars could correspond to a transient state where the viscoelastic response displays a plateau. Red and green curves of Fig. 2 indeed exhibit such transient stages whose duration ranges between about 10 Myr for the lower viscosity contrast (10^6, red curve) and about 100 Gyr for the larger one (10^{10}, green curve): these are likely to be relevant when computing dynamic topography over convective timescales. However, as illustrated by the blue curve, the transient stage also depends on the nature of the lithospheric viscosity structure: for a three layers case, as expected, two plateaus are observed. In this specific case, it is therefore difficult to compute a transient dynamic topography that is valid over a time range characteristic of convective motions. When the viscosity increase within the lithosphere is continuous (black curve of Fig. 2: viscosity profile built for $z_{lid} = 200$ km, see Fig. 1), the transient stage does not exhibit plateaus but a continuous relaxation of the topography over geological timescales.

In case of high viscosity contrasts, Zhong (2002) also showed that the steady-state response of VF-FS model is obtained after a time much longer than the time needed to reach the transient plateau with a viscoelastic formulation and slightly smaller than the time needed to reach the steady-state viscoelastic response. For example, in the two-layers case, the topography achieves $\sim$70 per cent of the steady-state value within 10^4 yr using the viscoelastic model, while the topography obtained with the VF-FS model reaches the steady-state value after 10^7 yr and, naturally, does not display the plateau of the transient viscoelastic response. This is outlined in Fig. 2, where the evolution of viscous topography is displayed with dashed lines. The time evolution is, in the case of the VS-FS model, entirely controlled by the longest characteristic time which depends on the viscosity of the top layer (Zhong 2002). Therefore, green and blue dashed lines in Fig. 2, both corresponding to a viscosity contrast of 10^{10}, are identical.

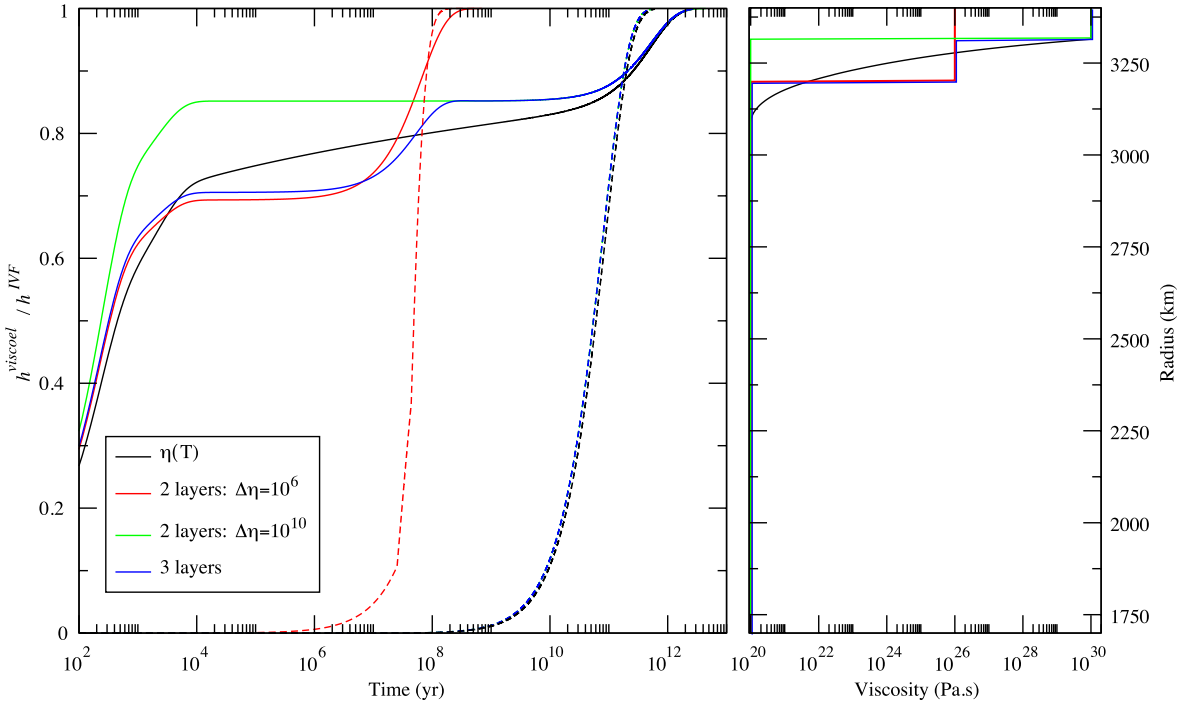

Figure 2. Time-dependent response of surface topography (left-hand panel) induced by a degree-2 load located at mid-depth for four different viscosity structures (right-hand panel). The following models are presented: viscoelastic (solid lines) and viscous with a free surface (VF-FS, dashed lines). All curves are normalized by the surface topography value obtained for the IVF model. The blue and green dashed lines are almost identical and their graphs overlap.

As indicated above, when a transient plateau in the topographic response is observed, it is possible to approximate the viscoelastic dynamic topography by elastic filtering of the viscous response, using either the IVF-TES model (e.g. Zhong 2002) or the ESW model (Golle *et al.* 2012). In the case of the IVF-TES model, the transient topography for a given degree ($h_\ell^{\rm viscoel}$) corresponds to a fraction of the steady-state (viscous) topography ($h_\ell^{\rm IVF}$) so that eqs (11)–(14) allow to compute the appropriate elastic thickness $T_{\rm e}$ for given rheological parameters (viscosity structure and shear modulus):

$$h_\ell^{\rm viscoel}(t) = C_\ell(T_{\rm e}) h_\ell^{\rm IVF}, \tag{15}$$

where expression for $C_\ell(T_{\rm e})$ is given by eq. (12). In the case of the ESW model, we compute the dynamic topography for increasing values of the elastic thickness, from 0 to 300 km, with an increment of 3.4 km (see Section 3.3). The best-fitting result to the viscoelastic dynamic topography at each time provides the viscous and elastic structures that best approximate the viscoelastic rheology.

Fig. 3 exhibits the elastic thicknesses predicted using IVF-TES (solid lines) and ESW (dashed lines) models, in order to approximate the viscoelastic deformation computed with the viscous structures depicted on the right-hand panel of Fig. 2. For the two-layers cases, the effective elastic thickness of the transient stage for the 201-km-thick lithosphere with a viscosity contrast of 10^6 (red curve) is equal to 210 km with the IVF-TES model and to 201 km with the ESW model. For the 82-km-thick lithosphere with a viscosity contrast of 10^{10} (green curve), the elastic thickness predicted using IVF-TES is $T_{\rm e} = 86$ km, whereas ESW predicts a closer value: $T_{\rm e} = 82$ km. Naturally, the case with three viscosity values (blue curve), displays two intermediate values for the effective elastic thickness and for a continuo us variation of lithospheric viscosity (black curve), the effective elastic thickness gradually decreases (from ∼180 km at 10^4 yr to ∼105 km at 10^9 yr), for both models.

To summarize, when the considered lithospheric viscosity structures are more complex than a two-values step-like profile, there is no such thing as an intermediate 'steady-state' relaxation corresponding to the shorter characteristic times of controlled by the viscosity mantle (Zhong 2002), that would be valid over geological timescales. Instead, a gradual relaxation should be expected for a continuous viscosity increase in the lithosphere.

4.2 Loads of other harmonic degrees located at mid-mantle depth and beneath the lithosphere

We then study the effect of the degree and of the depth of the load, as well as the effect of the lithospheric thickness on the transient viscoelastic topography, and therefore on the effective elastic thickness.

Step-like viscosity structure: In a first step, we compute the error made on the estimation of the transient viscoelastic topography using a step-like viscosity profile (lithospheric thickness of 201 km and viscosity contrast of 10^6, *cf.* red profile on the right-hand panel of Fig. 2) and the IVF model. The error is the difference between the IVF dynamic topography and the viscoelastic dynamic topography divided by the viscoelastic topography.

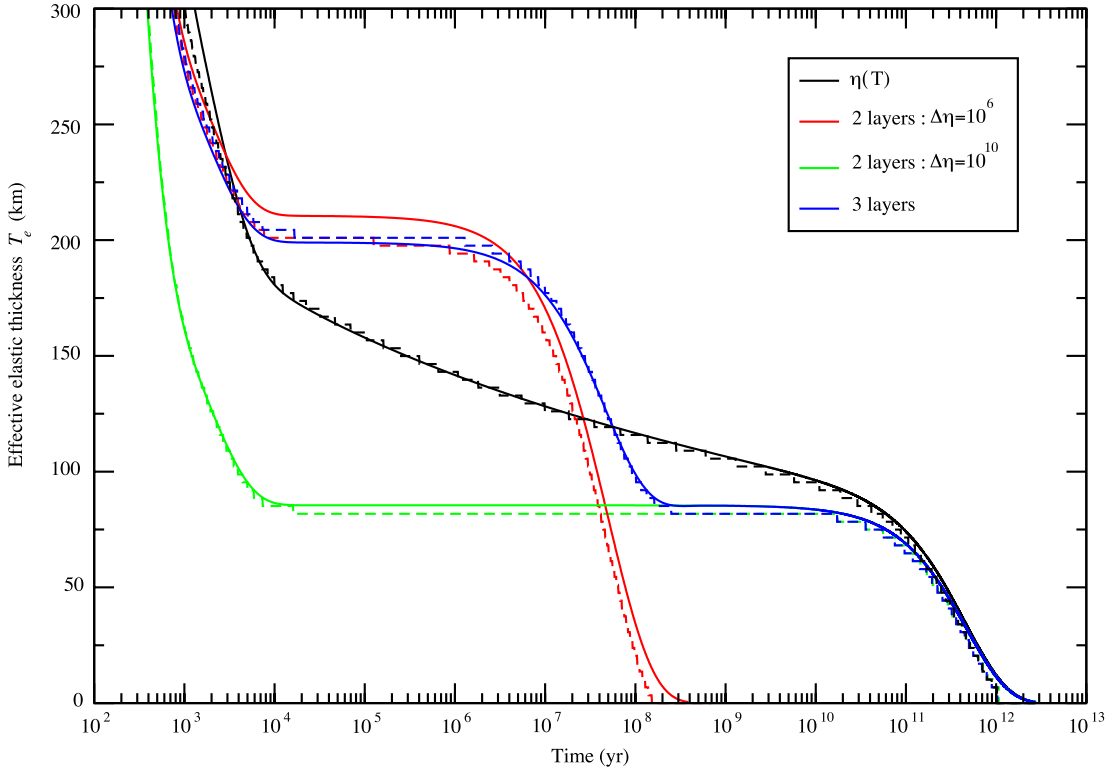

Figure 3. Effective elastic thickness T_e allowing to approximate the viscoelastic topography by filtering the instantaneous viscous response, for a degree-2 load at mid-depth, and for four different structures in viscosity, presented in the right-hand panel of Fig. 2. Solid lines represent results obtained using the IVF-TES model whereas dashed lines indicate results obtained using the ESW model.

Left-hand panel of Fig. 4 exhibits the errors associated with the evaluation of viscoelastic topographies at each degree when considering the viscous limit (IVF model) for a Mars-like body with the viscous structure presented above. As may be expected, the errors strongly decrease when time approaches the relaxation time. Errors at the plateau-like transient stage (which overlaps convective timescales) amount to 40–45 per cent for degrees 2–4 and reach 70 per cent for a degree-7 load. This model should thus not be used to model Mars dynamic topography. However, if the total radius of the body is increased, errors diminish: the right-hand panel of Fig. 4 shows the errors computed for a Venus-like planet with an identical viscous lithosphere of 201 km and associated with the IVF model for a mid-mantle depth load. Errors in determining topography are smaller than 5 per cent up to degree 7 but are already larger than 10 per cent at degree 11. Errors in the geoid will even be larger, therefore instantaneous viscous flow models should be used with caution when studying dynamic topography and geoid. In the following, we will focus on a Mars-sized body, the IVF model being particularly not appropriate for this planet.

Viscous models with elastic filtering are now used to approximate the viscoelastic transient topography. Left-hand panel (respectively right-hand panel) of Fig. 5 displays errors obtained with the IVF-TES model (respectively the ESW model). Errors for a given degree, are the smallest for the transient viscoelastic plateau. They naturally increase when the viscoelastic topography reaches its steady-state value. The filtered topography computed with IVF-TES compares very well with the transient viscoelastic one from degree 2 to 13 (error smaller than 5 per cent during the constant transient stage). However, the error increases with increasing degree and reaches approximately 50 per cent at degree 30. In contrast, ESW results yield small errors (less than 5 per cent), whatever the degree. The considered elastic thickness being the same ($T_e = 201$ km) for the two models, a first conclusion is that IVF-TES model does not apply in the context of a Mars-like body with an intermediate lithospheric thickness, for degrees larger than 13 and a mid-mantle depth load. Indeed, two sources of inaccuracy lie in the IVF-TES model: one is due to the elastic thin shell approximation (see Kalousová *et al.* 2012) whereas the other corresponds to the physical structure of the model (the IVF topography is applied as a surface load on the thin elastic shell). As a consequence, the error associated with each degree decreases with a decreasing ratio of the lithospheric thickness over the total radius. In the following, we only present results obtained with the ESW model, that couples the viscous and elastic shells. Being less accurate, the IVF-TES model will not be mentioned anymore in the following although, as previously mentioned, its simplicity of use and the possibility to extend the elastic thin shell approximation for a laterally varying elastic thickness make it an interesting alternative tool.

Continuous viscosity structure: When considering the viscosity structure derived from a stagnant lid thermal structure, as mentioned for a degree-2 load (see Section 4.1), the viscoelastic dynamic topography does not present any transient plateau, whatever the degree. Therefore, the effective elastic thickness that allows the best prediction of the viscoelastic dynamic topography, at each degree, varies with time. Fig. 6 displays these effective elastic thicknesses (as a function of degree and time) for three different viscosity structures ($z_{\rm lid} = 100$, 200 and 300 km, see viscosity profiles on the right-hand panel of Fig. 1) and for the time range 10^5 to 4×10^9 yr (considered to be the interesting time range for the convective processes). The load is located in the middle of the rheological sublayer below the lid (i.e. at a depth of $z_{\rm lid} + \delta$, *cf.* the

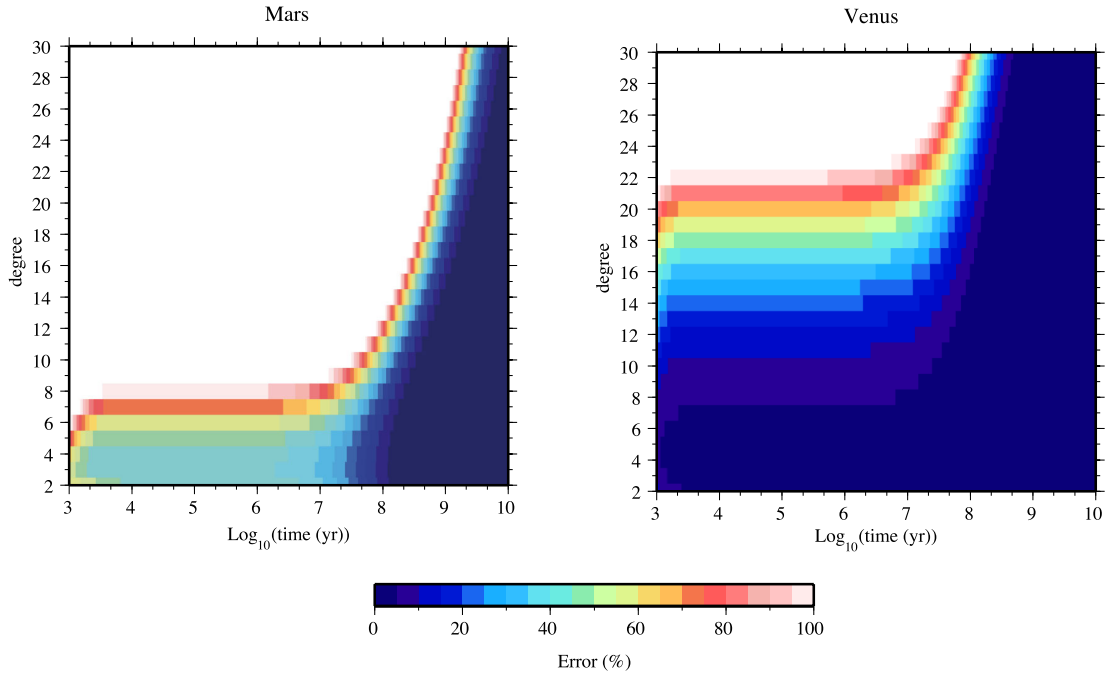

Figure 4. Time evolution of the errors (in per cent) as a function of degree associated with the approximation of the viscoelastic dynamic topography when using the instantaneous viscous flow model (IVF) for a Mars-like body (left-hand panel) and for a Venus-like body (right-hand panel). Viscosity equals 10^{26} Pa s in the viscous lithosphere (which is 201 km thick for both cases) and 10^{20} Pa s in the mantle beneath. The load is located at mid-mantle depth.

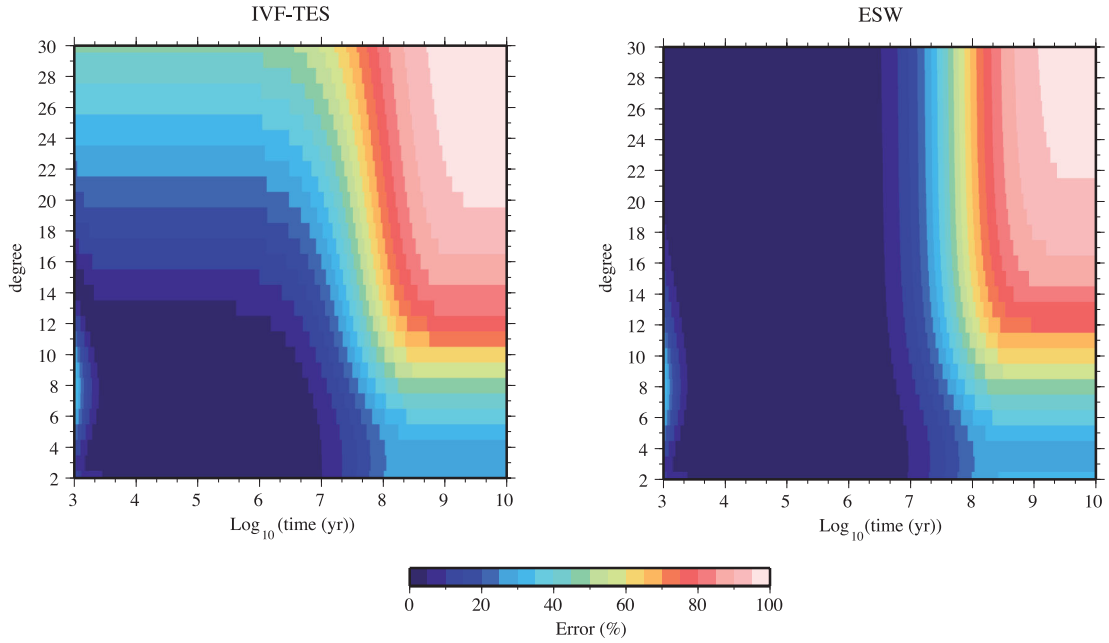

Figure 5. Time evolution of the errors (in per cent) as a function of degree associated with the approximation of the viscoelastic dynamic topography when using two different models: instantaneous viscous flow filtered with the elastic thin shell approximation (IVF-TES, left-hand panel) and a viscous shell coupled to an elastic shell within (ESW, right-hand panel). Viscosity equals 10^{26} Pa s in the viscous lithosphere (which is 201 km thick) and 10^{20} Pa s in the mantle beneath. The load is located at mid-mantle depth. Both models assume an elastic thickness of 201 km.

left-hand panel of Fig. 1). Note that, in the ESW model, each value of effective elastic thickness implies a different location for the evaluation of the traction applied at the base of the elastic shell ($z = T_e$). For a 100 km-thick lid, the effective elastic thickness varies from about 78 km at 10^5 yr to 51 km at 10^9 yr, for a 200-km-thick lid, from 160–170 to 99–102 km (depending on the degree), and for a 300-km-thick lid, from 238–252 to 146–150 km. For some specific degrees and over a specific time range, both depending on the viscosity structure (for example at degree 16 for a 300-km-thick lid), several values of the effective elastic thickness yield the same topography (hatched zones in right-hand and centre panels of Fig. 6). In this case, the preferred value is chosen so that the effective elastic thickness decreases with time (Fig. 7b illustrates this specific aspect and will be described in the next paragraph). Nevertheless, the results depicted in Fig. 6 are in good agreement

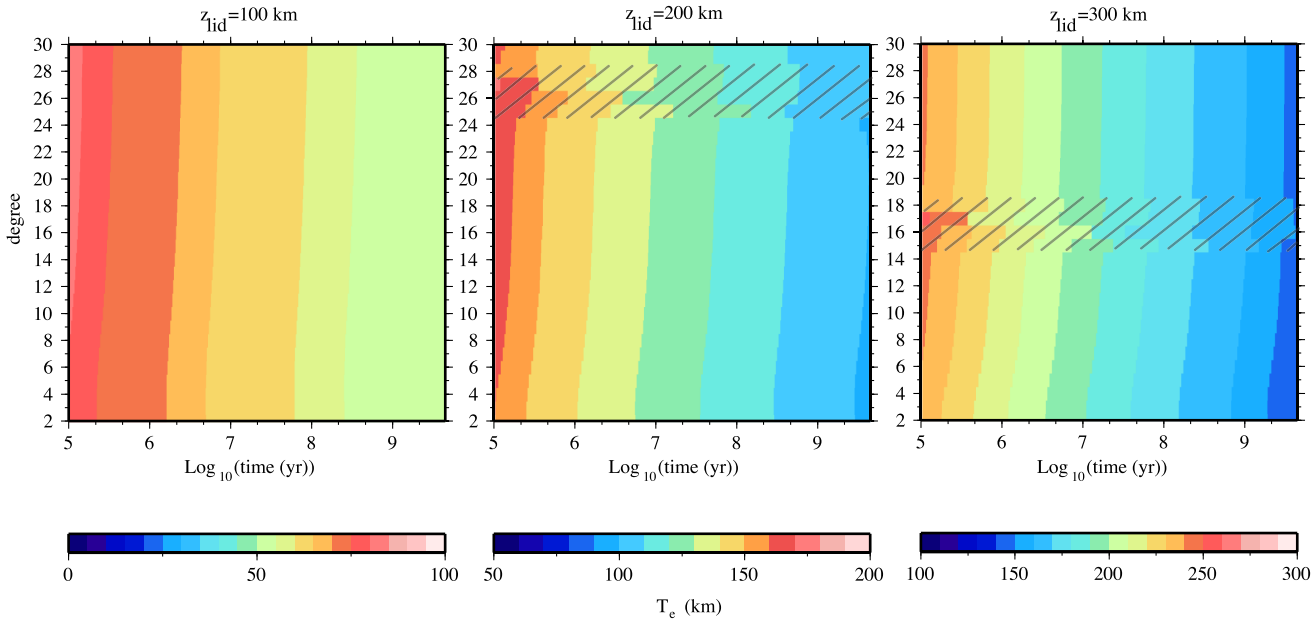

Figure 6. Effective elastic thickness that best predicts the viscoelastic topography using the ESW model, as a function of harmonic degree and loading time history. From left- to right-hand panel, results correspond to different viscosity structures ($z_{\rm lid}$ = 100, 200 and 300 km, see Fig. 1). Hatched areas depict zones where several values of effective elastic thickness yield a correct prediction of the viscoelastic topography (see text for further details). In this case, the effective elastic thickness is chosen so that it decreases with time (colour field in the hatched area). Results are obtained with a load located in the middle of the rheological sublayer below the rigid lid.

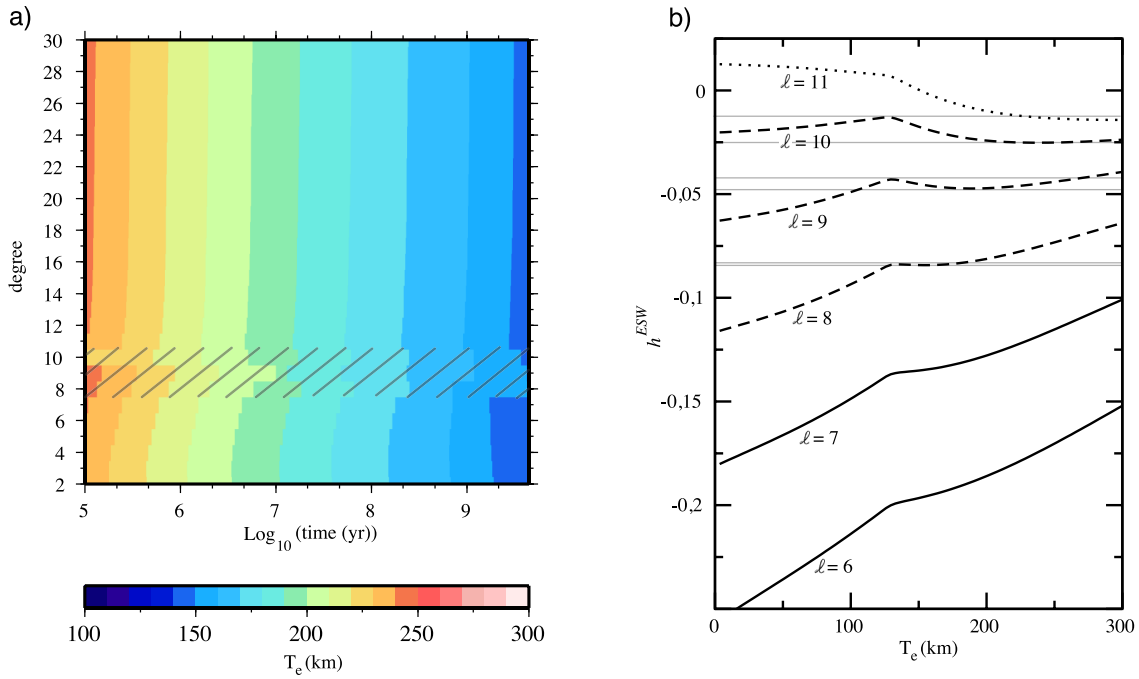

Figure 7. (a) Same as Fig. 6 for a 300-km-thick lid, but with a mid-depth load. (b) Topography predicted using the ESW model as a function of the effective elastic thickness included in the model, for harmonic degrees $\ell = 6$–11. For $\ell = 8$, 9 or 10 (dashed curves), a topography included between the two grey lines is obtained for several values of $T_{\rm e}$. This configuration is depicted on the left-hand panel by the hatched area. For $\ell = 6$ or 7 (solid curves) and $\ell = 11$ (dotted curve), each value of topography corresponds to a single value of $T_{\rm e}$.

with the thicknesses deduced from a rationale based on Maxwell times: any time value, if considered as a Maxwell time ($t = \eta_{\rm Max}/\mu$), can be associated with a Maxwell viscosity value $\eta_{\rm Max}$ above which the material behaves elastically. In turn, an elastic thickness can be deduced from the appropriate viscosity profile corresponding to the depth below which viscosity is smaller than the Maxwell viscosity. When considering such values of the elastic thickness based on the Maxwell time, errors on the topography are, for example, smaller than 1.5 per cent up to

degree 16 for the 300-km-thick lid. For higher degrees and specific narrow time ranges (corresponding to the change of sign of the viscoelastic dynamic topography), errors might be much larger. These discontinuous increases are linked to the radial discretization (the step in elastic thickness is of 3.4 km): the number of cells should be increased to reduce errors.

We now study the influence of the depth of the load on the effective elastic thickness that best models the viscoelastic topography. Fig. 7(a) corresponds to a case similar to the right-hand panel of Fig. 6 but a mid-depth load is considered. It shows that the best elastic thickness at a given time does not depend on the depth of the load with the exception of the hatched zone, where several values of elastic thicknesses lead to the same topography. Fig. 7(b) illustrates how the surface topography predicted by the ESW model evolves as the value of the effective elastic thickness T_e is varied. For degrees smaller than 8 (smaller than 15 if the load is located beneath the rigid lid, see right-hand panel of Fig. 6), the surface topography increases with increasing T_e (solid lines), while for degrees larger than 10 (larger than 18 for a load beneath the lid), it decreases with increasing T_e (dotted line). Consequently, in these two cases and in the range considered for T_e, a single value of effective elastic thickness will correctly predict the viscoelastic deformation. However, in the intermediate range of degrees (between 8 and 10 or 15 and 18 for a 300-km-thick lid, depending on the depth of the load), topography derived with the ESW model does not display a monotonous behaviour with T_e. Dashed curves on Fig. 7(b) show that, for $\ell = 8$, 9 or 10, any viscoelastic topography included between the two grey lines can be equally well predicted using two or three different values of the effective elastic thickness. Nevertheless, once again, errors associated with elastic thicknesses inferred from Maxwell times remain small (less than 0.8 per cent for degrees lower than 10 in the specific set-up of Fig. 7).

4.3 Synthetic plume

In order to illustrate the difficulties encountered in computing the surface dynamic topography using approximations of the viscoelastic deformation, we consider in the following a synthetic plume. The plume is arbitrarily located at the South pole of the sphere (so the deformation only depends on the harmonic degree ℓ and not on the order m). It has a constant width over the mantle and its density distribution follows a generalized Gaussian function with power 4:

$$\delta\rho_{\ell 0}(r) = 2\pi\rho_m\alpha\delta T \int_0^\pi P_{\ell 0}(\cos\theta)\exp\left[-\frac{1}{2}\left(\frac{\theta R_c}{\sigma_T r}\right)^4\right]\sin\theta\,\mathrm{d}\theta, \tag{16}$$

where the half-width σ_T of the Gauss function at the CMB is 20° and $P_{\ell 0}$ corresponds to the fully normalized associated Legendre functions. Fig. 8 depicts the distribution of the density anomaly coefficients $\delta\rho_{\ell 0}$ over radius and degree. The plume extends over the whole mantle up to the base of the rigid lid, and remains constant through the entire calculation. The density anomaly at the centre of the plume approximately corresponds to a deviation in temperature δT of 350 K compared to the surrounding mantle (thermal expansivity α is 3×10^{-5} K^{-1}). The spectral decomposition of the anomaly spreads over harmonic degrees 2–30, and topography and geoid are therefore computed over the same

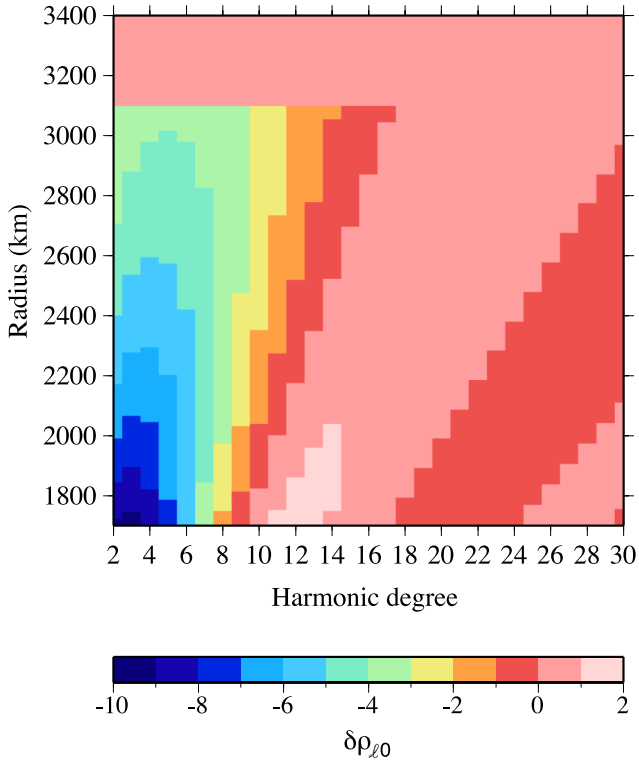

Figure 8. Distribution of the spherical harmonic coefficients of the density anomaly over radius and degree used in simulations with a synthetic plume. The spherical harmonics are normalized as in Golle *et al.* (2012).

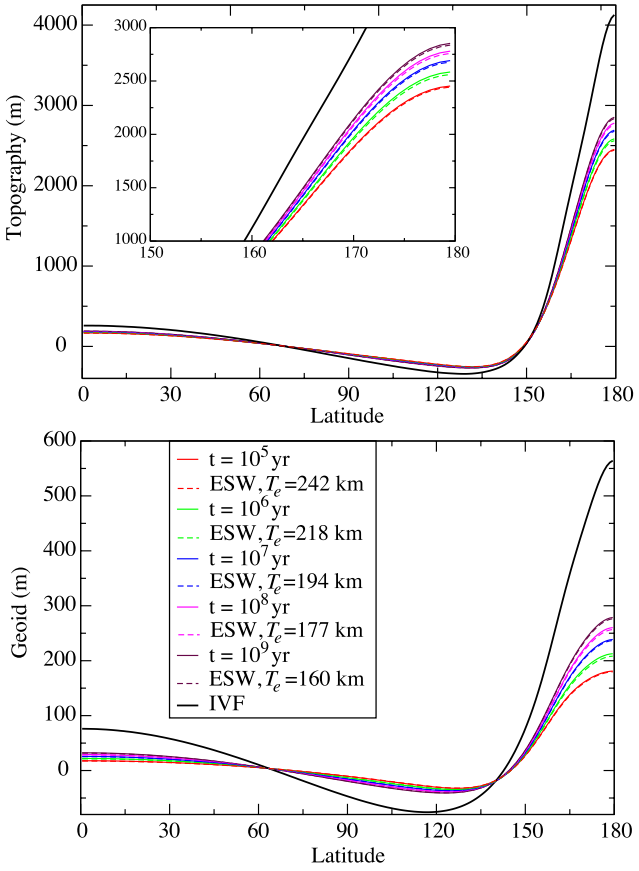

Figure 9. Dynamic topography (top panel) and geoid (bottom panel) profiles obtained with a synthetic stable plume after different loading time history ($t = 10^5$–10^9 yr). Viscous structure corresponds to the 300-km-thick rigid lid case (see green curve on right-hand panel of Fig. 1). IVF topography and geoid are displayed with thick black lines. The thickness of the elastic shell in the hybrid model (ESW) is deduced from the Maxwell viscosity, at each time (see text for further details). Results of the ESW model are represented with dashed lines.

range. We choose a temperature-dependent viscous structure of the lithosphere corresponding to a 300-km-thick stagnant lid (green line on the right-hand panel of Fig. 1).

Fig. 9 displays the viscoelastic dynamic topography (top panel) and geoid (bottom panel) profiles at various times and thus for various loading histories (10^5–10^9 yr) as solid colour lines and the instantaneous viscous topography and geoid as a black thick line. The IVF topography and the IVF geoid are much larger than the viscoelastic topographies, whatever the time. Indeed, after 10^5 yr, the viscoelastic topography is about 59 per cent of the IVF topography while the viscoelastic geoid is only 32 per cent of the geoid computed using IVF topography (69 per cent and 49 per cent, respectively after 10^9 yr). These results are similar to those obtained by Zhong (2002), where the author computed the transient viscoelastic topography and geoid above an axisymmetric plume and compared it to the IVF response. However, in contrast to our set-up, Zhong (2002) used a step-like viscous structure and therefore obtained a constant transient topography over large times. In order to compute the topography and geoid associated with an hybrid model (viscous and elastic shells coupled, ESW), we need to select a value for the elastic thickness. As demonstrated in the previous subsection, the equivalent elastic thickness varies with time, because the viscosity profile is continuous and not step-like. Results using elastic thicknesses evaluated at each time from the location of the Maxwell viscosity (as described above) are plotted with dashed colour lines on Fig. 9, and show a very good agreement with the viscoelastic topography and geoid. These conclusions illustrate the fact that, for a Mars-like body: (1) one needs to take into account the elastic filtering (as already concluded in Zhong 2002, for example), (2) considering realistic viscosity variations in the lithosphere (i.e. temperature dependent) induces a time-dependence of the thickness of the elastic shell in the hybrid model and (3) an hybrid model coupling the viscous and elastic shells (as the ESW model presented in Golle *et al.* 2012) has to be used, since the IVF-TES model does not apply for intermediate to thick viscous lithospheres if $\ell > 10$.

Of course, differences between the viscoelastic and the IVF responses will be smaller for a thinner lithosphere, and larger for a thicker lithosphere (see Fig. 10, left-hand panel stands for a 100-km-thick lid, and right-hand panel for a 500-km-thick one). For a Mars-like body with a 100-km-thick lithosphere (i.e. thinner than the lower range of estimate based on thermal evolution, e.g. Fraeman & Korenaga 2010), the geoid over a stable plume after 10^5 yr is lowered by 25 per cent when using the viscoelastic model compared to the IVF model, and by 19 per cent after 10^9 yr (note that this implies that the plume is stable during such a period). Differences increase considerably when considering a 500-km-thick rigid lid (geoid is lowered by more than 80 per cent, respectively more than 50 per cent, for a loading time history of 10^5 yr, respectively 10^9 yr).

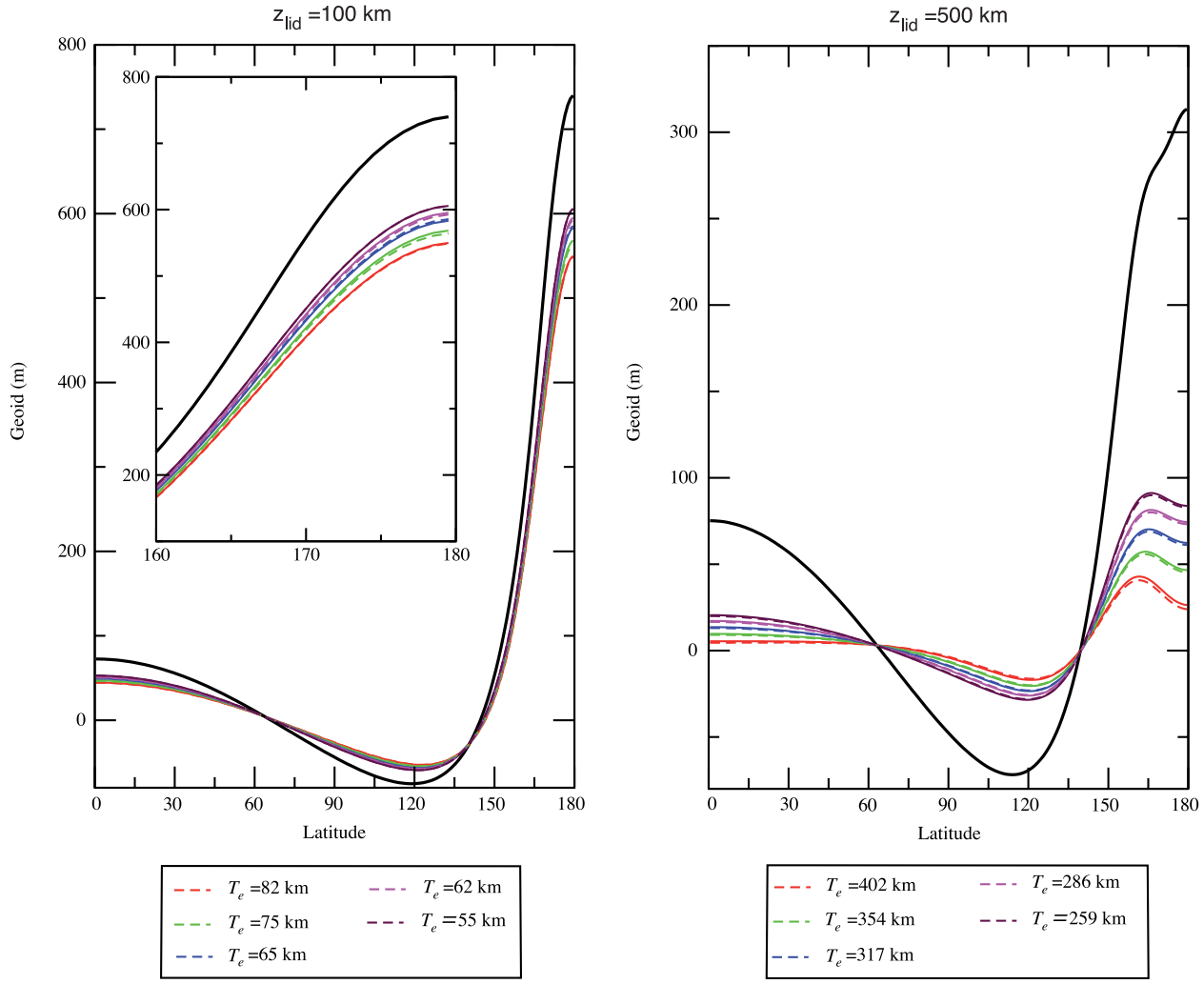

Figure 10. Geoid profile obtained with a synthetic stable plume after different loading time history ($t = 10^5$–10^9 yr). Viscous structure corresponds to the (left-hand panel) 100-km-thick rigid lid case (see black curve on right-hand panel of Fig. 1) and (right-hand panel) 500-km-thick rigid lid (see blue curve on right-hand panel of Fig. 1). Legend of solid lines is the same than for Fig. 9.

5 DISCUSSION AND CONCLUSIONS

The above tests investigate the validity domains of various approximations of viscoelastic deformation when trying to predict the dynamic topography and geoid. Four models involving viscous flow have been considered: (i) purely viscous flow (IVF model), (ii) purely viscous flow with a free surface (VF-FS) thus leading to a time dependency of the surface topography, (iii) viscous flow filtered by a thin elastic shell (IVF-TES) and (iv) viscous flow coupled with an elastic shell of finite thickness (ESW). A specific attention has been paid to the viscosity structure of the uppermost cold and possibly dry region of the mantle by considering either a strong but gradual decrease of viscosity with depth (corresponding to the thermal control of solid-state creep mechanisms) or a discontinuous jump (possibly corresponding to the dehydration of the lithosphere when compared to the bulk of the underlying mantle).

As shown earlier by Zhong (2002), for mechanical and geometrical parameters consistent with planetary objects, the time evolution of the viscoelastic topography can present a significant departure from the asymptotically relaxed shape obtained by the purely viscous instantaneous deformation (IVF). In the case of a discontinuous (step-like) viscosity structure, a transient stage preceding the final relaxation involves a plateau corresponding to the viscous relaxation of the flow in the less viscous mantle. For large viscosity contrasts the duration associated with this plateau probably implies that this transient stage is more pertinent on geological time scales than the steady-state topography. While the introduction of a free-surface in the viscous model (VF-FS) produces the correct time of occurrence for the steady-state dynamic topography, the latter does not capture the essence of viscoelastic topography during the transient stage. A simple method to describe the transient stage for a step-like viscous structure is to filter the viscous signal using the thin elastic shell coefficients introduced by Turcotte *et al.* (1981) (IVF-TES). We show that this approach is valid for small harmonic degrees but that large discrepancies can occur at higher degrees depending on the thickness of the lithosphere and the depth of the load. In the case of Mars, for a 200-km-thick lithosphere and a mid-mantle depth load, at a time after loading similar to characteristic convection timescales (10^6 yr for example), the IVF-TES approximation leads to errors on the topography that range from 0.38 per cent at degree 2 to ∼4 per cent at degree 12 and more than 20 per cent at degree 20. On the contrary, the

model involving the mechanical coupling of an elastic shell of finite thickness with the viscous flow (ESW) gives a good approximation, with the error only weakly increasing with the harmonic degree (errors from 0.08 per cent at degree 2, 1.1 per cent at degree 12 and 1.5 per cent at degree 20 for the same configuration). Note, however, that for planetary objects with a thinner lithosphere relative to the planetary radius, simpler approximations (such as IVF) could be valid up to high values of the harmonic degree. In the case of Venus, for a 200-km-thick lithosphere, the IVF solutions leads to errors of about 8 per cent for the topography and 11 per cent for the geoid at $\ell = 10$, while these are 21 and 26 per cent, respectively, at $\ell = 14$. These estimates naturally depend on the viscosity profile and of the depth of the loads.

In the case of a gradual decrease of viscosity with depth, compatible with a temperature-dependent rheology, the transient stage is characterized by a slow increase of the surface topography. We show that this more complex transient evolution can be modelled by introducing an elastic lithosphere whose thickness decreases with time. The elastic thickness at a given instant is simply the depth above which the viscosity is larger than the viscosity obtained assuming that the time of loading corresponds to a local Maxwell time. The application of such a procedure to Mars leads to errors in the predicted topography above the centre of a stable plume of less than 1 per cent for convective timescales (between 10^5 and 10^9 yr) and for a 300-km-thick rigid lid. For the same time range, the IVF model provides overestimations of the topography from 45 to 68 per cent. Errors in determining the geoid are larger but still reasonable when using the viscosity inferred by the Maxwell time to determine the effective elastic thickness and the ESW model (less than 2.2 per cent), whereas the IVF model leads to overestimations of 100–210 per cent. Naturally, these errors will be diminished for a thinner lid and increased for a thicker lid. In the case of Mars, the values considered in this study (100–500 km) for the average lithospheric thickness could actually represent the lower end of the present-day value: a recent assessment from thermal evolution models by Fraeman & Korenaga (2010) favours values approximately equal to 800 km. Given a typical thermal history, this result would imply that the average Martian lithosphere has been significantly thicker than 400 km during the last 3–4 Gyr of its evolution. Estimates of the effective elastic thickness on Mars by means of admittance and flexural models vary a lot among the studied region, from few tens of km to more than 100 km (e.g. McGovern *et al.* 2004; Belleguic *et al.* 2005) and even 300 km at the North pole (Phillips *et al.* 2008).

Obviously, the procedure described above in order to evaluate the time variation of the appropriate elastic thickness, based on the Maxwell time, depends on the time of emplacement of a given load and assumes a viscosity structure that remains constant through time. As such, it can only be applied to simplified dynamic contexts and can hardly be generalized to a system where time-dependent convection will produce multiple loads at various instants nor to transient evolutions where the lithospheric structure significantly varies.

Finally, two distinct viscosity structures have been considered in this study to model (1) the thermal lithosphere, and (2) a dehydrated lithosphere (in our models, the amplitude of the viscosity jump is much larger than plausible values). A real planetary lithosphere will involve both contributions: the thermal evolution of the lithosphere as well as the outgassing history of the planet could provide successively highly distinct lithospheric structures. The parameterized model proposed by Fraeman & Korenaga (2010) who explicitly consider this coupled evolution, allows to envision that the early history of Mars is characterized by a depleted stiff lithosphere whose final thickness is reached in less than 1 Gyr. The value of this thickness possibly exceeds at first the one of the thermal lithosphere. This situation would correspond to a step-like viscosity increase located below or in the lowermost part of the stagnant lid (where a gradual viscosity decrease occurs with depth). Later on, the thermal lithosphere thickens while the thickness of its dehydrated part remains unchanged. At the same time, the mantle is more and more degassed so that the amplitude of the viscosity jump between the dehydrated lithosphere and the mantle below it decreases.

To conclude, our results indicate that the various approximations of viscoelastic dynamic topography are valid only for specific ranges of wavelengths, viscosity structures, and thicknesses of the planetary lithosphere: when considering very viscous lithospheres, the IVF model will only be suitable for thin lithospheres compared to the planetary radius and at low harmonic degrees; the IVF-TES model may be used for thicker lithospheres and low degrees, while the ESW model is appropriate whatever the viscous structure and the degree, as long as the effective elastic thickness can be computed from the loading and thermal history.

ACKNOWLEDGEMENTS

We thank Scott King and Shijie Zhong for their very constructive reviews. We also thank Shijie Zhong for sharing his results in order to benchmark our code. This work has been partly supported by the ANR MadMacs and by the Charles University mobility fund. Caroline Dumoulin acknowledges support from the French Space Agency (CNES) through the Inter Disciplinary Scientist (IDS) role of Christophe Sotin on the Venus Express mission.

REFERENCES

Belleguic, V., Lognonné, P. & Wieczorek, M., 2005. Constraints on the Martian lithosphere from gravity and topography data, *J. geophys. Res.,* **110,** E11005, doi:10.1029/2005JE002437.

Benešová, N. & Čížková, H., 2012. Geoid and topography of Venus in various thermal convection models, *Stud. Geophys. Geod.,* **56,** 621–639.

Beuchert, M. & Podladchikov, Y., 2010. Viscoelastic mantle convection and lithospheric stresses, *Geophys. J. Int.,* **183,** 35–63.

Beuthe, M., 2008. Thin elastic shells with variable thickness for lithospheric flexure of one-plate planets, *Geophys. J. Int.,* **172,** 817–841.

Čadek, O. & Fleitout, L., 2003. Effect of lateral viscosity variations in the top 300 km on the geoid and dynamic topography, *Geophys. J. Int.,* **152,** 566–580.

Fraeman, A. & Korenaga, J., 2010. The influence of mantle melting on the evolution of mars, *Icarus,* **210,** 43–57.

Gerya, T. & Yuen, D., 2007. Robust characteristics method for modelling multiphase visco-elasto-plastic thermo-mechanical problems, *Phys. Earth planet. Inter.,* **163,** 83–105.

Golle, O., Dumoulin, C., Choblet, G. & Čadek, O., 2012. Topography and geoid induced by a convecting mantle beneath an elastic lithosphere, *Geophys. J. Int.,* **189,** 55–72.

Harder, H., 1991. Numerical-simulation of thermal-convection with Maxwellian viscoelasticity, *J. Non-Newton. Fluid Mech.,* **39,** 67–88.

Harder, H., 2000. Mantle convection and the dynamic geoid of Mars, *Geophys. Res. Lett.,* **27,** 301–304.

Harder, H. & Christensen, U., 1996. A one-plume model of martian mantle convection, *Nature,* **380,** 507–509.

Hirth, G. & Kohlstedt, D.L., 1996. Water in the oceanic upper mantle: implications for rheology, melt extraction and the evolution of the lithosphere, *Earth planet. Sci. Lett.,* **144,** 93–108.

Huang, J., Yang, A. & Zhong, S., 2013. Constraints of the topography, gravity and volcanism on venusian mantle dynamics and generation of plate tectonics, *Earth planet. Sci. Lett.,* **362,** 207–214.

Jordan, T.H., 1978. Composition and development of the continental tectosphere, *Nature,* **274,** 544–548.

Kalousová, K., Souček, O. & Čadek, O., 2012. Deformation of an elastic shell with variable thickness: a comparison of different methods, *Geophys. J. Int.,* **190,** 726–744.

Karato, S., 2010. Rheology of the deep upper mantle and the implications for the longevity of the continental roots: a review, *Tectonophysics,* **481,** 82–98.

Kaus, B. & Becker, T., 2007. Effects of elasticity on the Rayleigh-Taylor instability: implications for large-scale geodynamics, *Geophys. J. Int.,* **168,** 843–862.

Korenaga, J. & Karato, S.-I., 2008. A new analysis of experimental data of olivine rheology, *J. geophys. Res.,* **113,** B02403, doi:10.1029/2007JB005100.

Kraus, H., 1967. Thin elastic shells: an introduction to the theoretical foundations and the analysis of their static and dynamic behavior, Wiley.

Lowry, A. & Zhong, S., 2003. Surface versus internal loading of the Tharsis rise, Mars, *J. geophys. Res.,* **108,** 5099, doi:10.1029/2003JE002111.

Martinec, Z., 2000. Spectral-finite element approach to three-dimensional viscoelastic relaxation in a spherical earth, *Geophys. J. Int.,* **142,** 117–141.

McGovern, P.J. *et al.*, 2004. Correction to "Localized gravity/topography admittance and correlation spectra on Mars: implications for regional and global evolution", *J. geophys. Res.,* **109,** E07007, doi:10.1029/2004JE002286.

Muhlhaus, H.-B. & Regenauer-Lieb, K., 2005. Towards a self-consistent plate mantle model that includes elasticity: simple benchmarks and application to basic modes of convection, *Geophys. J. Int.,* **163,** 788–800.

Phillips, R.J. *et al.*, 2008. Mars North Polar deposits: stratigraphy, age, and geodynamical response, *Science,* **320,** 1182–1185.

Redmond, H.L. & King, S.D., 2004. A numerical study of a mantle plume beneath the Tharsis Rise: reconciling dynamic uplift and lithospheric support models, *J. geophys. Res.,* **109,** E09008, doi:10.1029/2003JE002228.

Redmond, H.L. & King, S.D., 2007. Does mantle convection currently exist on Mercury?, *Phys. Earth planet. Inter.,* **164,** 221–231.

Reese, C., Solomatov, V. & Baumgardner, J., 2005. Scaling laws for time-dependent stagnant lid convection in a spherical shell, *Phys. Earth planet. Inter.,* **149,** 361–370.

Ricard, Y., 2007. Physics of mantle convection, *Treat. Geophys.,* **7,** 31–87.

Ricard, Y., Fleitout, L. & Froidevaux, C., 1984. Geoid heights and lithospheric stresses for a dynamic Earth, *Ann. Geophys.,* **2,** 267–286.

Richards, M. & Hager, B., 1984. Geoid anomalies in a dynamic Earth, *J. geophys. Res.,* **89,** 5987–6002.

Roberts, J. & Zhong, S., 2004. Plume-induced topography and geoid anomalies and their implications for the Tharsis rise on Mars, *J. geophys. Res.,* **109,** E03009, doi:10.1029/2003JE002226.

Schmalholz, S., Podladchikov, Y. & Schmid, D., 2001. A spectral/finite difference method for simulating large deformations of heterogeneous, viscoelastic materials, *Geophys. J. Int.,* **145,** 199–208.

Sleep, N.H., 2003. Survival of archean cratonal lithosphere, *J. geophys. Res.,* **108,** 2302, doi:10.1029/2001JB000169.

Turcotte, D.L., Willemann, R., Haxby, W. & Norberry, J., 1981. Role of membrane stresses in the support of planetary topography, *J. geophys. Res.,* **86**(B5), 3951–3959.

Wieczorek, M.A., 2007. The gravity and topography of the terrestrial planets, *Treat. Geophys.,* **10,** 165–206.

Willemann, R.J. & Turcotte, D.L., 1982. The role of lithospheric stress in the support of the Tharsis Rise, *J. geophys. Res.,* **87,** 9793–9801.

Wu, P. & Peltier, W.R., 1982. Viscous gravitational relaxation, *Geophys. J. R. astr. Soc.,* **70,** 435–485.

Zhong, S., 2002. Effects of lithosphere on the long-wavelength gravity anomalies and their implications for the formation of the Tharsis rise on Mars, *J. geophys. Res.,* **107**(E7), 5054, doi:10.1029/2001JE001589.

Zhong, S. & Roberts, J., 2003. On the support of the Tharsis Rise on Mars, *Earth planet. Sci. Lett.,* **214,** 1–9.

Zhong, S., Gurnis, M. & Moresi, L., 1996. Free-surface formulation of mantle convection—I. basic theory and application to plumes, *Geophys. J. Int.,* **127,** 708–718.

Zhong, S., Paulson, A. & Wahr, J., 2003. Three-dimensional finite-element modelling of Earth's viscoelastic deformation: effects of lateral variations in lithospheric thickness, *Geophys. J. Int.,* **155,** 679–695.